

Mitigating urban–rural disparities in humid-heat risks in China

Received: 23 May 2024

Accepted: 3 December 2025

Published online: 23 December 2025

Chuwei Liu¹, Siyu Chen¹✉, Jianping Huang¹, Xuhui Lee², Chao Zhang¹, Keer Zhang¹, Lulu Lian¹, Yunchao Jiang³, Xingxing Tu³, Nan Yin³, Runbin Zhang³ & Danfeng Wang¹

 Check for updates

Global warming is intensifying compound humid-heat threats, yet long-term risk assessments accounting for urban–rural disparities remain scarce. In this study, we develop a comprehensive risk assessment framework by integrating the Intergovernmental Panel on Climate Change risk approach with indicators from the United Nations Sustainable Development Goals related to humid-heat mitigation and adaptation. Applying this framework to China from 2001 to 2020, we find that sustainable development progress substantially reduces vulnerability, particularly in urban areas, leading to a decline in humid-heat risk. In contrast, rural areas show a slower vulnerability reduction compared to urban areas and show no statistically significant change in humid-heat risk, despite a narrowing urban-rural risk gap. Regional disparities in sustainable development are key drivers of risk heterogeneity in both urban and rural settings. Our findings underscore the urgency of coordinated urban-rural development to simultaneously advance sustainable development and climate adaptation.

Global warming is exacerbating thermal extremes across the globe, which poses severe threats to human health¹. The combined effects of high temperature and humidity present particularly severe risks, as they critically impair the human body's ability to regulate its temperature through evaporative cooling². Humid-heat, quantified by wet-bulb temperature (T_w), has already reached or exceeded 35 °C in some coastal subtropical locations, a threshold approaching the limits of human survivability³. East Asia has experienced particularly significant increases in humid-heat. Between 2001 and 2020, 91.5% of meteorological sites in the Northern Hemisphere recorded humid heatwaves that started earlier or ended later compared to 1981–2000 period, with East Asia and Southeast Asia being especially affected⁴. In East Asia, these humid heatwaves are projected to begin as early as March and extend into October⁴.

Extreme humid-heat represents one of the most dangerous natural hazards, having caused tens of thousands of fatalities in several extreme events so far this century^{5,6}. The impacts of these events

extend far beyond immediate mortality, manifesting as systemic societal impacts. Extreme humid-heat causes serious labor losses^{7,8}. Impaired cognitive and physical performance across various sectors currently results in over 650 billion hours of annual labor losses globally⁸. These productivity declines translate into substantial economic burdens, with estimated annual global costs reaching 2.1 trillion (in 2017 purchasing power parity-adjusted international dollars) due to humid-heat-induced workforce incapacitation⁸. By the mid- to late-century, global population exposure to deadly humid-heat is projected to increase by a factor of five to ten⁹, with densely populated regions possessing less developed infrastructures likely to bear a disproportionate share of this burden^{9,10}.

While numerous heat risk assessments have been conducted across countries of different income levels^{11–13} as defined by the World Bank based on the Gross National Income per capita in 2024¹⁴, they have largely focused on extreme temperatures while neglecting the synergistic effects of humidity. Moreover, research on humid-heat risk

¹Collaborative Innovation Center for Western Ecological Safety, College of Atmospheric Sciences, Lanzhou University, Lanzhou, China. ²School of the Environment, Yale University, New Haven, CT, USA. ³College of Earth and Environmental Sciences, Lanzhou University, Lanzhou, China.

✉ e-mail: chensiyu@lzu.edu.cn

remains limited, especially regarding differences between urban and rural areas. The role of urban and rural vulnerability in extreme humid-heat events has not been sufficiently examined.

Under the dual pressures of global warming and increasing human activities, China is facing growing humid-heat risks. Over the past 60 years, the average summer T_w has increased by 0.21°C per decade¹⁵, exposing large populations to hazardous humid-heat. Rapid urbanization has further intensified the spatial differentiation of these risks. Between 2010 and 2020, China's urbanization rate increased from 49.7% to 63.9%¹⁶. This rapid land-use transformation has triggered coupled effects of urban heat island and dry island¹⁷⁻¹⁹. In response, China has implemented extensive measures to mitigate the negative impacts of rapid climate change, including poverty eradication, improved healthcare, infrastructure strengthening, and enhanced monitoring and early warning systems^{20,21}. Nonetheless, substantial disparities in social development persist between urban and rural regions across China. These gaps directly influence residents' capacity to deal with humid-heat, adding complexity to the assessment of such risks nationwide.

There is a need to develop a refined humid-heat risk assessment framework capable of accurately capturing the differences in risk between urban and rural areas in China. It would inform the formulation of health protection strategies and the advancement of climate-adaptive development. To formulate and implement targeted policies that enhance climate resilience and safeguard human health, the following questions must be addressed: What are the key disparities in humid-heat hazards, population exposure and social vulnerability between urban and rural areas? How have China's policies, aligned with the United Nations Sustainable Development Goals (SDGs), influenced humid-heat risks in these contexts? What are the spatiotemporal patterns of humid-heat risk in urban and rural China over the past two decades?

In this study, we investigate the spatiotemporal evolution of extreme humid-heat events across China from 2001 to 2020 and assess the associated integrated risks in both urban and rural regions. By adopting the risk assessment framework established by the Intergovernmental Panel on Climate Change (IPCC) and augmenting it with key SDGs indicators related to humid-heat mitigation and adaptation, we account for hazard, vulnerability, and exposure, with particular emphasis on the crucial role of adaptive capacity in mitigating these risks. Furthermore, we investigate the temporal trends and spatial heterogeneity of humid-heat risks, highlighting how divergent sustainable development pathways influence the urban-rural disparities in risk profiles. This work provides a scientific foundation for formulating coordinated urban-rural sustainable development strategies aimed at alleviating climate risks against the backdrop of global warming.

Results

Significant increase in wet-bulb temperature

China experienced a marked rise in T_w from 2001 to 2020 (Fig. 1a), driven by combined increases in temperature and vapor pressure. This rising trend is modulated by multiple factors, such as climatic and anthropogenic influences^{22,23}, leading to severe population exposure. Using a hazardous T_w threshold of 27 °C^{24,25}, we found that nearly half of the urban population and one-third of rural residents were exposed to humid-heat hazards during the summer over the past two decades (Supplementary Fig. 1). Notably, temperate and continental climate zones (Supplementary Fig. 2) showed the most pronounced T_w increases, reaching 0.27°C per decade (Fig. 1b), with accelerated warming observed between 2016 and 2020 (Supplementary Fig. 3). Tropical climate zone recorded the highest T_w , followed by temperate climate zone (Supplementary Fig. 3a). The majority of these regions are strongly influenced by the East Asian monsoon, which transports substantial moisture^{26,27} and is a key driver of the higher T_w compared to other climate zones. With the exception of arid climate zone,

temperatures in all other climate zones increased significantly. In temperate climate zone, T_w increase resulted from the combined effects of rising temperature and vapor pressure (Supplementary Fig. 4). Urban areas exhibited significantly higher T_w than rural regions, particularly in temperate and continental climate zones, where urban-rural differences reached 2.9 °C and 2.7 °C, respectively (Supplementary Fig. 5). In highly urbanized areas, factors such as reduced vegetation, increased impermeable surfaces, and higher anthropogenic heat emissions are observed²⁸⁻³⁰, which contribute to localized warming.

The variation of T_w percentiles exhibited distinct features. Urban areas exhibited higher values compared to rural areas across the entire distribution, from the lower to the upper percentiles (Fig. 1c and d). In both urban and rural China, the 90th and 70th percentiles of T_w were concentrated primarily in southern China. Urban T_w increased by 0.33 °C and 0.25 °C per decade, respectively, compared to corresponding rural increases of 0.30 °C and 0.18 °C (Fig. 1e), reflecting a heightened susceptibility of urban areas to extreme humid-heat events. Conversely, rural areas experienced a more rapid increase in median T_w (0.31 °C per decade at the 50th percentile) than urban areas (0.11 °C per decade; Fig. 1e). This divergence was most pronounced along the Hu Huanyong Line (Supplementary Fig. 6), where slower urbanization and weaker anthropogenic thermal influences moderated temperature changes. The increase in rural T_w was primarily driven by a rapid increase in vapor pressure (Supplementary Fig. 7a). This rise may be related to expanded vegetation cover (Supplementary Fig. 7b), which played a crucial factor in regulating local climate conditions. At lower percentiles (30th and 10th), the lower baseline temperatures constrained the potential for vapor pressure increases, thereby narrowing urban-rural differences in T_w trends.

Declining urban vulnerability reducing urban-rural risk gap

Humid-heat risk across China was assessed using a humid-heat risk index (HHRI; Fig. 2a). The HHRI is composed of three component indices (Fig. 2b-d; see Methods): the hazard index (HI), which quantifies humid-heat severity based on the number of days exceeding the T_w threshold (27 °C); the vulnerability index (VI), derived from SDG indicators for humid-heat mitigation and adaptation; and the exposure index (EI), representing population exposure. The results reveal pronounced spatial-temporal divergence between urban and rural China. Although urban regions generally faced higher risks (Fig. 2a), urban-rural HHRI disparities narrowed significantly in 68.2% of Chinese regions between 2001 and 2020 (Fig. 3a-d). High-risk urban areas were concentrated in the middle-lower Yangtze River basin and South China, whereas high-risk rural areas extended further northwards into Shandong, collectively forming persistent risk belts across eastern China (Supplementary Fig. 8).

To analyze the risk components, regions with HHRI, HI, VI, and EI values in the top 25% of their overall distributions were defined as high-HHRI, high-HI, high-VI, and high-EI, respectively. Between 2001 and 2020, the proportion of urban areas with high-HHRI decreased significantly from 44.9% to 26.5% (Fig. 3a). Conversely, the proportion of high-HHRI rural areas increased from 5.8% to 11.3% (Fig. 3b). The most notable narrowing of the urban-rural HHRI gap occurred in central and eastern China, especially in the temperate climate zone of Hunan province, where the disparity decreased at a rate of 0.06 per decade (Fig. 3c and d). However, South China experienced similar increases in HHRI in both urban and rural areas (Fig. 3a, b), resulting in no significant reduction in the urban-rural gap (Fig. 3c and d).

The urban-rural HHRI gap narrowed primarily due to a more rapid decline in urban vulnerability. The urban VI decreased at a rate of 0.31 per decade, which was faster than the rural decline of 0.20 per decade (Fig. 2b). This indicated that areas with high-VI were eliminated in urban areas of central and western provinces (e.g., Henan, Guizhou, and Ningxia) after 2011 (Fig. 3e). Through sustainable development

efforts, rural areas reduced the coverage of high-VI from 75% in 2001 to nearly zero (Fig. 3f). Nevertheless, systematically building resilience was hindered by their slower economic growth compared to urban areas and an aging population³¹, which consequently led to a significant widening of the urban-rural VI gaps across 79.5% of regions in China (Supplementary Fig. 9). Notably, HHRI patterns differed across climatic zones within the same province. For example, Sichuan's temperate zone exhibited a substantially higher HHRI than the continental zone, particularly in urban areas, with a 20-year average difference of 0.09 (Fig. 3a).

The widening of China's urban-rural VI gap is reflected in the disparities observed in humid-heat-related SDGs (Supplementary Fig. 10a). Specifically, urban areas demonstrated stronger performance in SDG1 (No Poverty; Supplementary Fig. 10b) and SDG3 (Good Health and Well-Being; Supplementary Fig. 10c), whereas rural areas showed comparative advantage in SDG12 (Responsible

Consumption and Production; Supplementary Fig. 10d) and SDG13 (Climate Action; Supplementary Fig. 10e). Notably, the urban-rural gap in SDG1 continued to widen at an annual rate of 3.9%, underscoring deepening disparities in access to economic opportunities. Meanwhile, urban areas consistently outperformed rural areas in SDG3 attainment. This disparity stemmed mainly from the higher proportion of vulnerable populations in rural areas, where population aging remains a key bottleneck to achieving this goal (Supplementary Fig. 11). These spatial differences highlight distinct transformation paths. Urban vulnerability reduction is driven by rapid economic development and improved healthcare, while rural areas show unique advantages in sustainable production and climate adaptation practices.

Despite improvements in urban VI, increases in heat hazard (HI, rising by 0.20 per decade) and population exposure (EI, increasing by 0.08 per decade) impeded further decline in HHRI

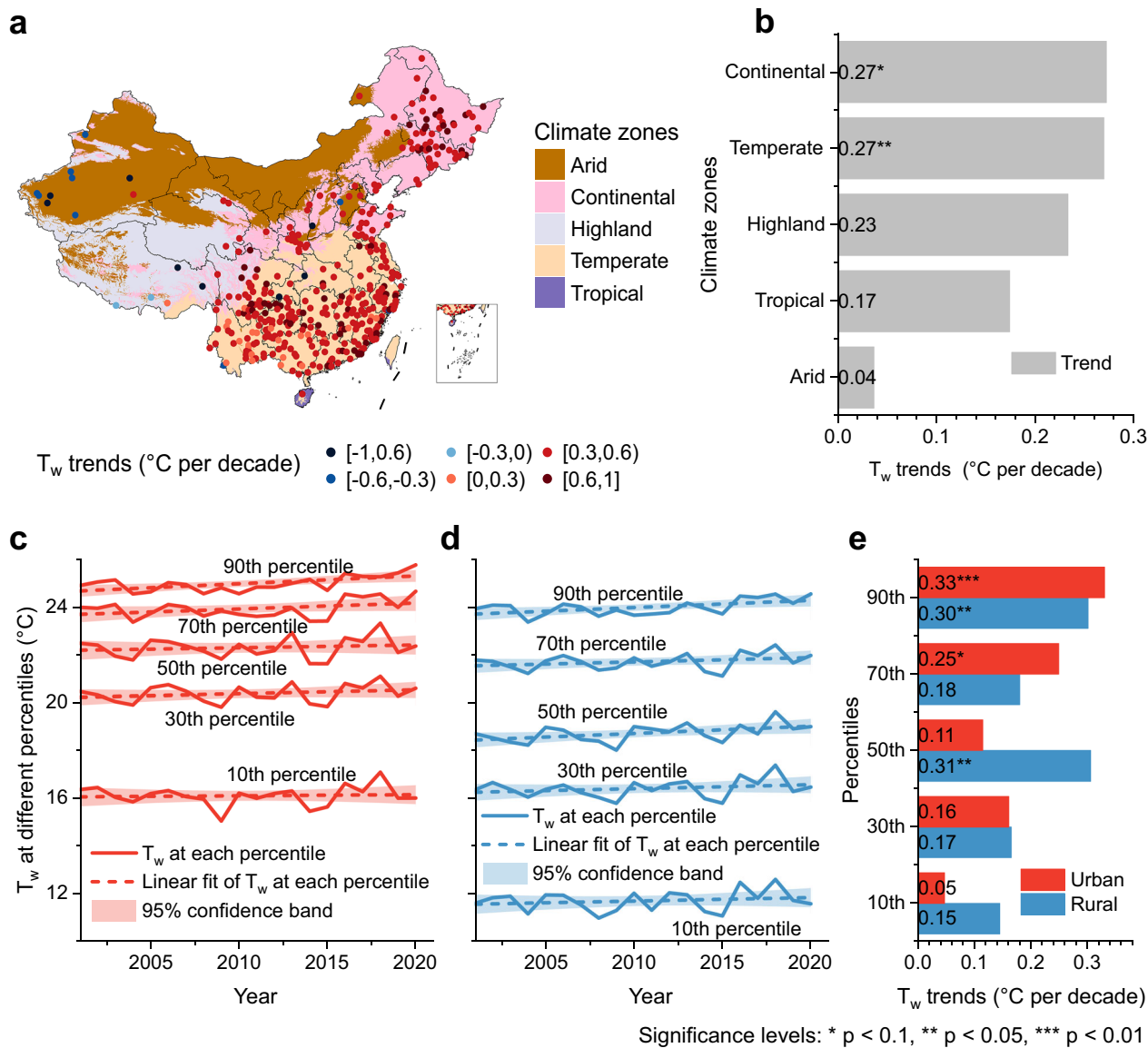


Fig. 1 | Wet-bulb temperature (T_w) across China from 2001 to 2020. **a** T_w trends at in-situ stations with statistically significant trends ($p < 0.1$). Colors on the map indicate the climate zones, with purple, amber, light orange, pink, and light lavender representing the tropical, arid, temperate, continental, and highland climate zones, respectively. The climate zoning data were obtained from ref. 41. This figure uses base map data adopted from ref. 47, available under the MIT license on GitHub (<https://github.com/ruiduobao/shengshixian.com>).

across different climate zones. **c** T_w at 10th, 30th, 50th, 70th, and 90th percentiles for urban areas. **d** The same as panel c but for rural areas. The solid lines represent T_w at different percentiles, while the dashed lines represent the linear fits. Shaded areas around the dashed lines represent the 95% confidence bands. **e** T_w trends per decade in urban and rural areas at different percentiles (10th, 30th, 50th, 70th, and 90th). Significance levels are indicated with * $p < 0.1$, ** $p < 0.05$, and *** $p < 0.01$.

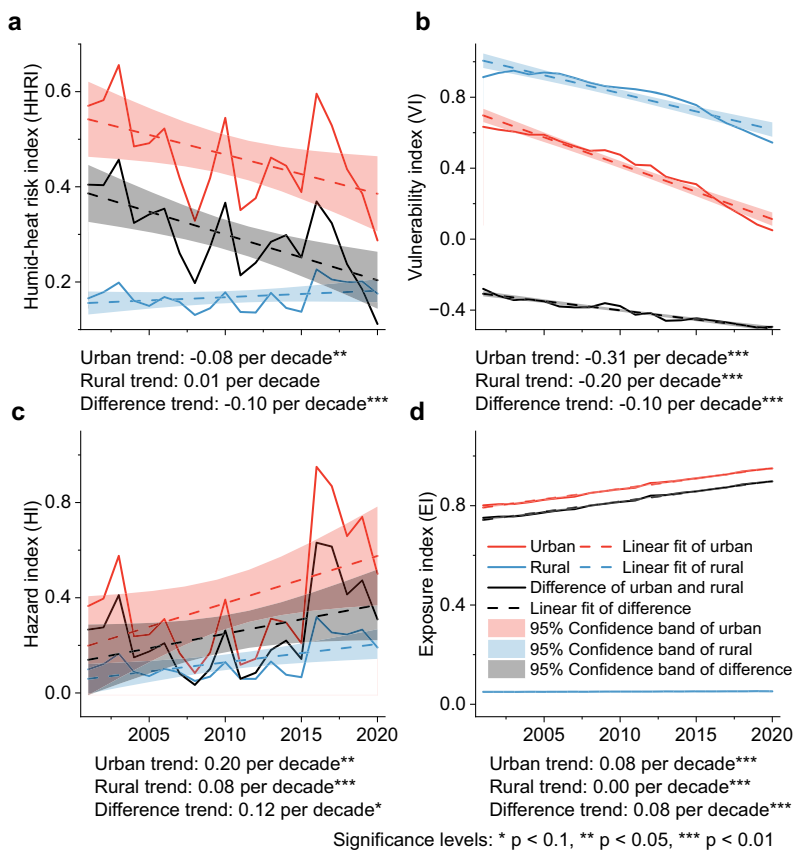


Fig. 2 | Humid-heat risk index (HHRI), vulnerability index (VI), hazard index (HI) and exposure index (EI) for urban and rural areas from 2001 to 2020. a HHRI; **b** VI; **c** HI; **d** EI. The solid red and blue lines represent the values of urban and rural areas, respectively, while the solid black lines represent the urban-rural difference

(urban value minus rural value). The dashed red, blue, and black lines represent the linear fits for the values of urban, rural, and urban-rural difference, respectively. The red, blue, and black shadings around the dashed lines represent 95% confidence bands. Significance levels are indicated with * $p < 0.1$, ** $p < 0.05$, and *** $p < 0.01$.

(Fig. 2c and d). From 2001 to 2020, 52% of urban areas experienced high-HI, and 64% experienced high-EI, either as single or compound risk patterns. These areas were mainly concentrated in eastern coastal (e.g., Shanghai and Zhejiang) and central (e.g., Hunan and Jiangxi) regions (Fig. 3e), spatially coinciding with the expansion of urban heat islands and population aggregation. In urban areas across central, eastern coastal, and southern China, the dominant risk pattern began as a compound of high-HI and high-EI, transitioned through a single high-EI phase, before returning to a compound state (Fig. 3e), due to the fluctuations in HI and the continuous increase in EI (Supplementary Fig. 12). Additionally, urban areas in the continental climate zone of Jilin and Gansu, as well as the temperate zone of Shaanxi, consistently exhibited a high-EI risk pattern over 20 years, while other climate zones within these provinces did not (Fig. 3e), reflecting uneven population distribution in these regions. Although rural areas largely avoided high-EI (Fig. 3f), approximately 38% of rural regions were exposed to high-HI threats, either as single or compound risks, during 2001–2020.

This spatial heterogeneity reflects the differences in the risk regulation pathways of urban and rural China. Urban areas intensify heat exposure and environmental stress due to high-intensity human activities, but reduce vulnerability through infrastructure improvement to lower the risk. Rural areas require enhanced vulnerability reduction to bolster resilience against growing climate pressures.

Spatial risk heterogeneity driven by development disparities

Research on the heterogeneity of sustainable development and its impact on humid-heat risks provides critical insights for mitigating humid-heat risks and understanding the complex drivers of spatio-temporal urban-rural risk disparities across diverse climatic zones. We defined regions with high-HHRA as extremely high humid-heat risk areas (EHHRA), visualized spatially in Supplementary Fig. 13. EHHRA were stratified by recent composite SDG scores into high (30%; defined as High-SDGS), medium (40%; defined as Middle-SDGS), and low (30%; defined as Low-SDGS) sustainability groups. Our analysis focused on the interplay of key factors: economic development (reflected in SDG1), indicative of the material capacity to adapt to humid-heat conditions; health and well-being (reflected in SDG3), as better healthcare and a population less vulnerable to humid-heat stress are more resilient; sustainable resource use (reflected in SDG12), promoting green development; and climate action (reflected in SDG13), enabling proactive mitigation. We further explored how humid-heat risk changed in regions with different sustainable development under the influence of these factors in both urban and rural EHHRA.

In urban EHHRA, generally, regions with high SDG scores exhibited lower HHRI, particularly within continental and temperate climate zones (Fig. 4a). For instance, in continental climate zone, High-SDGS regions such as Beijing, Tianjin, and several northern provincial capitals (Supplementary Fig. 13) demonstrated higher EI values than other regions (Fig. 4a). However, these regions showed stronger performance in poverty eradication, as reflected in SDG1 (Supplementary

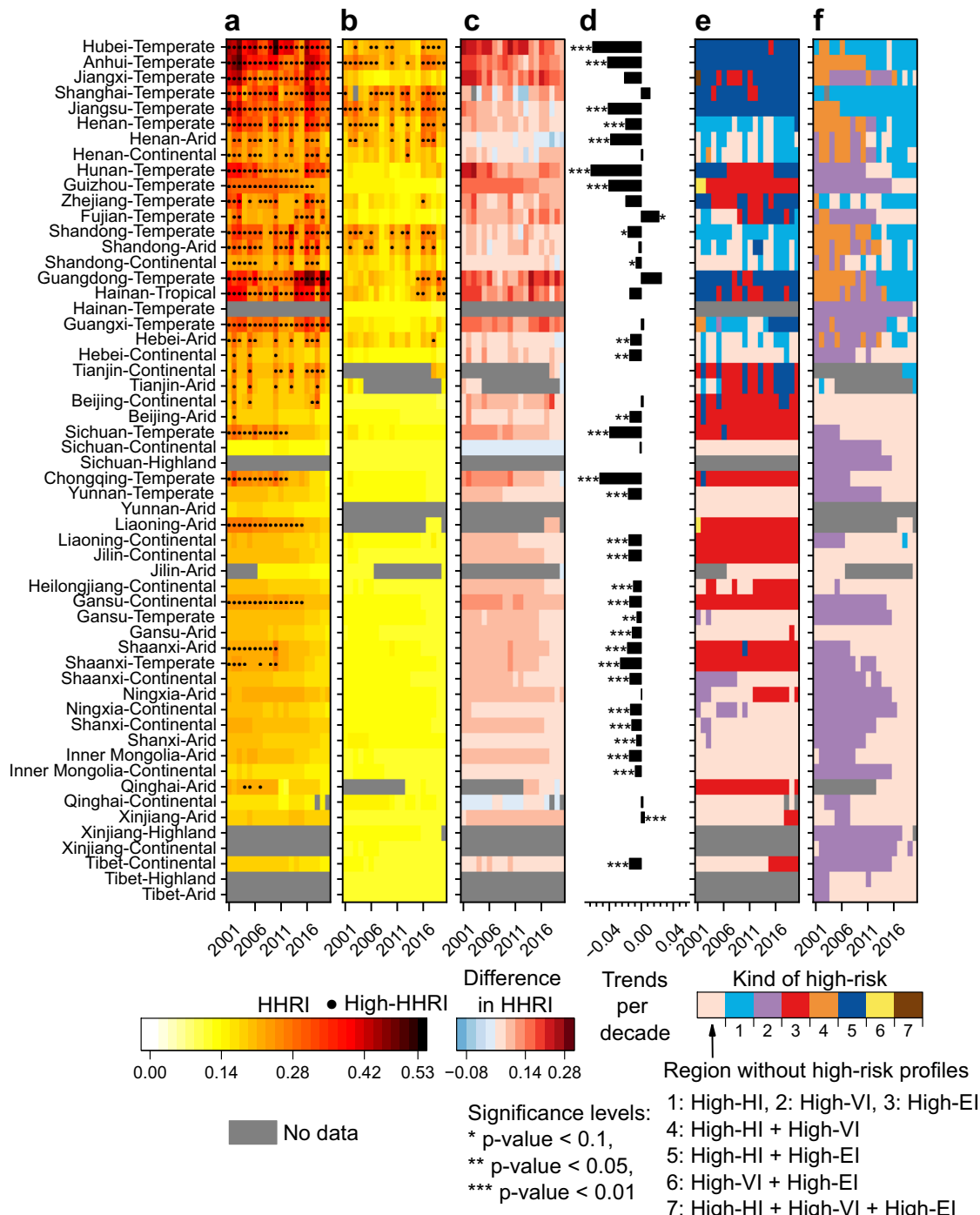


Fig. 3 | Urban and rural humid-heat risk index (HHRI), urban-rural HHRI difference, and urban and rural high-risk profiles across province-climate zone combinations in China from 2001 to 2020. **a** HHRI in urban areas, with color representing the range from low to high. **b** HHRI in rural areas, using the same color scale as in panel **a**. For panels **a** and **b**, the black dots indicate years and regions with high-HHRI, defined as those HHRI values in the top 25% of their overall

d Trends per decade in urban-rural HHRI difference. Significance levels are indicated with $*p < 0.1$, $**p < 0.05$, and $***p < 0.01$. **e** Risk profiles in urban areas. **f** Risk profiles in rural areas. High-risk profiles are categorized as: 1, high-HI; 2, high-VI; 3, high-EL; 4, high-HI combined with high-VI; 5, high-HI combined with high-EL; 6, high-VI combined with high-EL; and 7, high-HI combined with high-VI and high-EL.

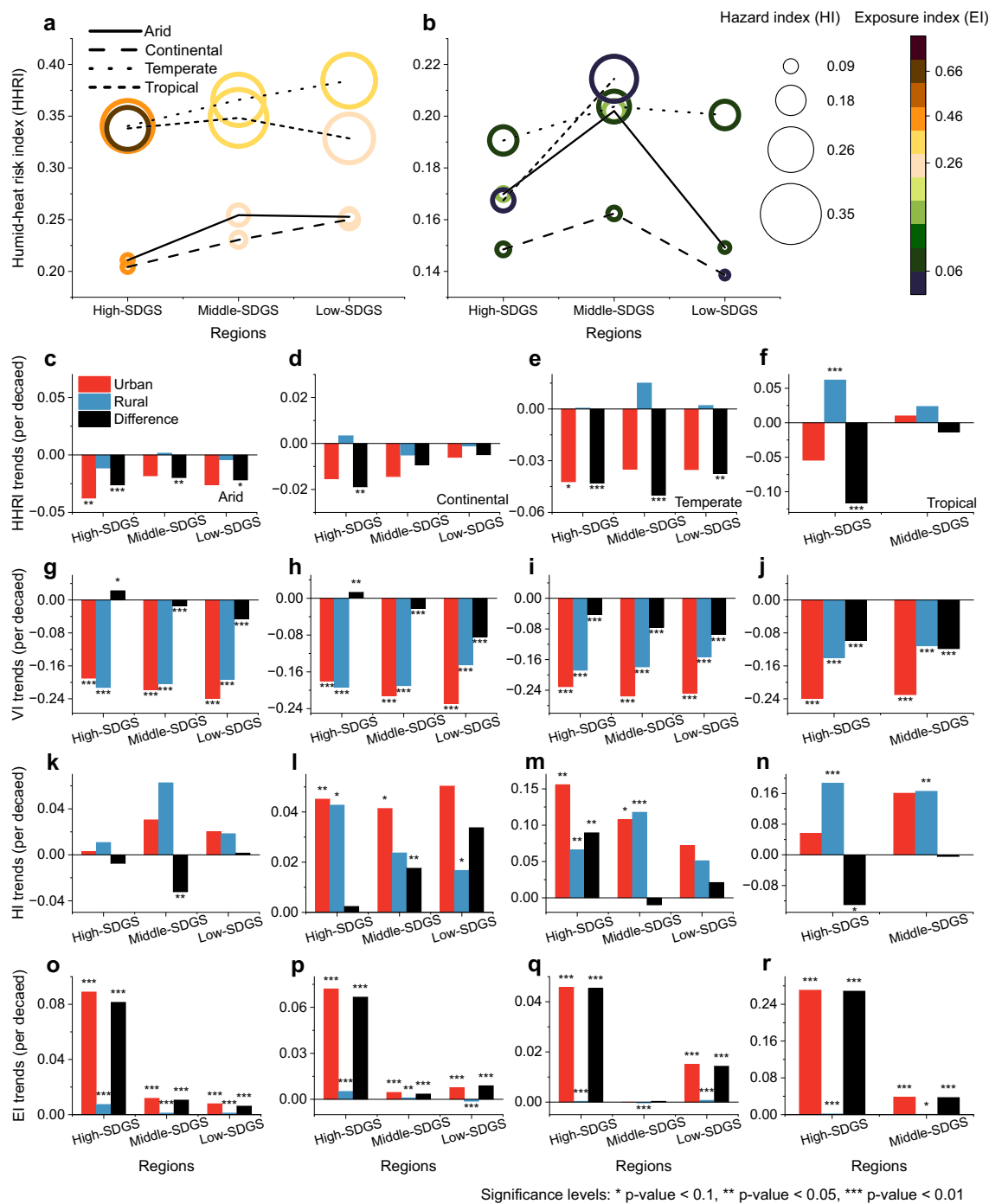


Fig. 4 | Urban and rural humid-heat risk index (HHRI), vulnerability index (VI), hazard index (HI) and exposure index (EI) of extremely high humid-heat risk area (EHHRA) and urban-rural difference (urban value minus rural value).

a HHRI (Y-axis), HI (shape size), and EI (color) values for regions with high (High-SDGS), middle (Middle-SDGS), and low (Low-SDGS) SDG scores across different

climatic zones in urban areas. b The same as panel a, but for rural areas. c-f Trends of HHRI in arid, continental, temperate, and tropical climatic zones, showing urban areas (red bars), rural areas (blue bars) and urban-rural differences (black bars). g-j Trends of VI in the above climatic zones. k-n Trends of HI in the above climatic zones. o-r Trends of EI in the above climatic zones.

Fig. 14), effectively mitigating risk accumulation in high-exposure environments. Their HHRI values remained lower than those observed in Middle- and Low-SDGS regions (Fig. 4a). In urban areas, HHRI declined by 0.02–0.05 per decade in High-SDGS regions. In contrast, Middle- and Low-SDGS regions exhibited a more modest decline (e.g.,

northern Hebei, southern Gansu, and some regions in central China, as shown in Supplementary Fig. 13 (Fig. 4c–f). Consequently, Middle- and Low-SDGS regions exhibited 10% and 11% higher mean HHRI relative to High-SDGS regions across urban EHHRA. Notably in arid and tropical zones, HHRI spatial differentiation was driven by HI disparities.

Specifically, in arid zones, HI in Middle-SDGS regions exceeded that in High- and Low-SDGS regions by 56% and 19%, respectively. Similarly, in tropical zones, it exceeded the other two groups by 31% and 15%, respectively. This uneven distribution of HI resulted in the highest HHRI value in the Middle-SDGS region in these two climate zones (Fig. 4a).

In rural EHHRA, Middle-SDGS regions exhibited the highest HHRI values. Specifically, HHRI values in these regions were 7%–28% and 2%–35% higher than in High- and Low-SDGS regions, respectively (Fig. 4b). This is due to the fact that High-SDGS regions maintained lower EI, driven by higher social development, resulting in lower HHRI. In contrast, Low-SDGS regions, with slower population growth, had the lowest EI (Fig. 4b), effectively reducing HHRI. Middle-SDGS regions lacked the sustainable development advantages of High-SDGS regions and faced higher EI and HI than Low-SDGS regions, leading to the highest HHRI values (Fig. 4b). These areas were constrained by lagging social development and population issues, while facing growing humid-heat hazards, resulting in significantly higher HHRI compared to other regions. This highlights the need for more focused policy intervention and resource allocation in these areas.

In addition, rural VI in High-SDGS regions declined faster than in other regions, with a decline across the four climate zones that was 2–25% and 10–34% higher than in Middle- and Low-SDGS regions, respectively, leading to smaller urban-rural differences in the rate of VI decline (Fig. 4g–j). This indicated more balanced urban-rural development in High-SDGS regions, helping to mitigate the increase in humid-heat risk. For High-SDGS regions in arid and continental climate zones, such as Beijing, Tianjin, and several provincial capitals (e.g., Xi'an in Shaanxi province and Shijiazhuang in Hebei province; see Supplementary Fig. 13), urban-rural coordination was particularly effective, with rural VI declining more than urban VI (Fig. 4g and h). However, rural areas in High- and Middle-SDGS regions generally exhibited faster HI growth than those in Low-SDGS regions (Fig. 4k–n), while High-SDGS regions also experienced rapid increases in urban EI (Fig. 4o–r). These combined trends pose new challenges for risk management.

Discussion

To reveal the differences in urban-rural humid-heat risks and their driving factors in China, this study developed an assessment framework of HHRI that integrated the IPCC risk assessment approach with localized SDG indicators. Through this framework, we systematically examined how the humid-heat hazard, social vulnerability and population exposure in urban and rural areas evolved and jointly influenced the spatiotemporal variations in comprehensive humid-heat risk across different regions. It investigated mitigation and adaptation capabilities, with a focus on how inter-regional differences in sustainable development shaped social vulnerability, and how social vulnerability drove HHRI variation. Overall, advancements in sustainable development in China effectively reduced urban vulnerability, against the backdrop of increases in both humid-heat hazards and population exposure, leading to an overall decline in HHRI in urban areas. However, the decrease in rural vulnerability was less pronounced than in urban areas, with no significant reduction in HHRI. This result highlights the urgent need for coordinated urban-rural development and provides scientific insights for the global efforts to address climate risks.

The urban outcomes provide a key reference, demonstrating that while improved social adaptation with sustainable development does not completely eliminate HHRI, it can create conditions that significantly reduce it by enabling residents to better cope with humid-heat stress. Despite progress in reducing vulnerability, a major challenge persists in urban areas in the form of simultaneously rising hazards and exposure. With urbanization, the concentration of population in urban areas increases exposure risks, while intensified human activities also exacerbate heat hazards^{32–34}. For rural areas, prioritizing vulnerability reduction is the key to lowering HHRI.

Specifically, lower economic growth and more severe aging compared to urban areas are the main limitations to the reduction of vulnerability, which also represent the main challenges in rural sustainable development.

Significant differences in climate conditions and sustainable development exist across regions in China, leading to notable spatial heterogeneity in humid-heat risks. Central China, the southeastern coastal regions, and South China are primarily located in temperate climate zone. These areas are highly urbanized, densely populated³⁵, and serve as key drivers of China's economic development³⁶. However, they also represent critical areas for humid-heat risks. Effective management of risks in these regions is of utmost importance. Northwest China, including provinces such as Shaanxi, Ningxia, and Gansu, should also be of concern. These areas are characterized by higher social vulnerability, indicating lower risk adaptation capacities compared to other regions. It is crucial to prioritize measures, such as strengthening infrastructure, improving social services, and enhancing emergency response capabilities, to better equip them for coping with extreme climate events. Regardless of climate conditions, rural areas in High-SDGS regions showed more significant VI declines, suggesting more balanced urban-rural development in these areas, which helped mitigate the negative impacts of extreme humid-heat.

In summary, this contributes to a comprehensive and detailed understanding of the variations and long-term evolution in humid-heat risks across urban and rural areas in China, within the context of differences in sustainable development. Additionally, it offers insights for rapidly urbanizing countries facing similar challenges in balancing climate change and development. Achieving balanced urban-rural development and jointly reducing climate risks calls for a dual strategy. This strategy involves revitalizing rural economies and demographic revitalization, while optimizing urban spatial structures to mitigate population exposure and the urban heat island effect.

This paper has the following limitations. First, the assessment framework does not fully include micro-social factors, such as community governance capacity and individual behavioral differences, potentially underestimating the adaptive potential of local areas. Additionally, the urban-rural division, based on Moderate Resolution Imaging Spectroradiometer (MODIS) retrievals, with a resolution of 500 m, might not fully capture the complexity of urban-rural transition zones. In these zones, the complexity of mixed land use contributes to a more diverse and variable microclimate. Moreover, in our study, we assigned equal weights to HI, VI and EI to maintain neutrality and balance. Since these three belong to different, incomparable dimensions, equal weighting prevents anyone factor from being over-emphasized, thus maintaining fairness in the model. Maintaining equal weighting in interdisciplinary research ensures a unified framework, preventing misunderstandings from subjective differences in weight assignment. Future research may explore adaptive weighting strategies to further refine risk assessments.

Methods

Calculation of the wet-bulb temperature

The wet-bulb temperature describes the combined effects of temperature and humidity and has been established as an effective comprehensive indicator reflecting heat stress and extreme heat^{15,24}. It is based on the balance between the latent heat of wet-bulb evaporation and the sensible heat from the environment. The formula for calculating the wet-bulb temperature²⁴ is given by Eq. (1):

$$T_w = T + \frac{e - e_s^*(T_w)}{\gamma}, \quad (1)$$

where T_w and T are wet-bulb temperature and air temperature, respectively, e and e_s^* are actual and saturation vapor pressure, respectively, and γ is the humidity constant, which depends on air

pressure and temperature. The numerical methods provided in the R package Bigleaf were employed to solve for T_w ³⁷.

The meteorological observation data were sourced from the Resource and Environmental Science Data Platform, managed by the Institute of Geographic Sciences and Natural Resources Research, Chinese Academy of Sciences. We ensured the station's stable presence in urban or rural areas with continuous observational data from 2001 to 2020. Such stable stations, defined as those with consistent observations over 20 years and always located within urban or rural regions, were utilized to calculate the temporal variations of T_w in China, as well as the 20-year trends of T_w at each station. This approach also helped to capture the most representative climatic characteristics of urban and rural areas. To ensure the reliability of the data, stations with fewer than 27 observed days per month, which account for less than 90% of the total observation days, were excluded from the analysis. The 3σ criterion, a common statistical method for outlier detection^{38,39}, was initially applied for identifying suspicious data, followed by verification. These observation stations only cover mainland China, so our study is also limited to mainland China.

Building upon previous work⁴⁰, the annual land cover type data (MCD12Q1 v061) from the MODIS satellite retrievals (<https://lpdaac.usgs.gov/products/mcd12qv061/>) from 2001 to 2020 with 500 m spatial resolution were employed to delineate urban and rural areas. The land use classification followed the International Geosphere-Biosphere Programme (IGBP) land cover classification scheme. Pixels classified as urban and built-up areas in the IGBP scheme were defined as urban zones. To accurately capture population exposure to humid-heat risks, rural areas were designated as non-urban regions excluding three uninhabited land types: water bodies, permanent snow and ice, and barren. In addition, the Köppen climate classification was employed to delineate China's climate zones. Using the classification map for 1991–2020⁴¹, China was categorized into tropical, arid, temperate, continental, and highland climate zones (Supplementary Fig. 2).

Selection of sustainable development goals and scoring calculation

We selected 4 SDGs closely related to the response to humid-heat from among the 17 SDGs: SDG1 (No Poverty), SDG3 (Good Health and Well-Being), SDG12 (Responsible Consumption and Production) and SDG13 (Climate Action). Based on these 4 SDGs, we selected 8 social-ecological indicators for China's specific context (Supplementary Table 1). The value of each social-ecological indicator was normalized to a standard range (0–100), with a higher normalized value indicating better performance⁴². The normalized individual scores for positive and negative social-ecological indicators (Supplementary Table 1) were calculated by Eq. (2) and Eq. (3), respectively:

$$X' = \frac{X - MIN_X}{MAX_X - MIN_X} \times 100, \quad (2)$$

$$X' = \frac{MAX_X - X}{MAX_X - MIN_X} \times 100, \quad (3)$$

where X' is the normalized individual score for a given social-ecological indicator, X is the original value of the social-ecological indicator, and MIN_X and MAX_X are the minimum and maximum values of the social-ecological indicators, respectively.

The score of each SDG was calculated as the average of the normalized individual scores of its corresponding indicators. Additionally, we computed the average score across the 4 SDGs. We summarized the annual values of urban and rural areas in mainland China from 2001 to 2020, reflecting the dynamic changes in sustainable development. In stratifying the EHHRA regions into High-, Middle-, and Low- SDGs groups, the composite SDG scores from the past few years (2018–2020) were used to better reflect the current level of sustainable

development in each region. For details on the indicators and data sources that constituted the SDGs, refer to Supplementary Table 1.

Humid-heat risk assessment

The risk assessment framework draws on previous work assessing climate risks^{12,43}. A framework for risk assessment in which risk is a function of hazard, exposure, and vulnerability was provided by the IPCC in its Fifth Assessment Report (AR5)⁴⁴. Hazard refers to a physical event or phenomenon that may cause damage⁴⁴. Vulnerability refers to the susceptibility and ability of a system, community or individual to respond to hazards due to physical, social, economic and environmental factors⁴⁴. Exposure refers to the presence and location of humans or other affected objects (such as ecosystems, physical assets, etc.) in front of danger⁴⁴. The higher the exposure, the greater the frequency and intensity of the hazards.

Based on the framework of AR5, we selected indicators to evaluate risks from three aspects: hazard, vulnerability, and exposure. In our work, they represent the severity of the humid-heat, the ability to adapt to and cope with the humid-heat, and the population's exposure, respectively. We calculated the HI, VI and EI of humid-heat to quantify the risks in these three aspects. Based on the three aspects mentioned above, we carried out assessments of humid-heat risks from 2001 to 2020, separately at the national and regional levels in mainland China, and distinguished urban and rural areas.

The risk assessment framework in our work combined the IPCC AR5 risk assessment framework with localized SDG indicators, and established a comprehensive evaluation system that covered climatic, socioeconomic, and policy dimensions. The HHRI is defined as a composite metric derived from the product function of three fundamental components: HI, VI and EI. Compared with the additive principle, the multiplicative principle can better reflect the nonlinear interactions among system components⁴³, reflecting the compounding effects of humid-heat stressors. The HHRI is calculated by Eq. (4):

$$HHRI = \sqrt[3]{HI \times VI \times EI}. \quad (4)$$

Calculation of hazard index, vulnerability index and exposure index

A threshold of 27 °C was used^{24,25}, and if the daily T_w reached or exceeded this value, the day was considered to experience humid-heat hazards. The cumulative number of area-weighted hazard days during the summer in the target region is used to characterize the humid-heat hazards.

We overlaid the tertiary-level of the Köppen classification with prefecture-level cities to obtain detailed zoning. For urban areas (C-CUs) and rural areas (C-CRs) with observation stations of the detailed zone, we calculated their daily average T_w . The number of summer hazardous humid-heat days ($N_{hazardous}$) for urban or rural areas was calculated by area-weighted averaging, with C-CU (or C-CR) as the basic unit. The formula is given by Eq. (5):

$$N_{hazardous} = \frac{\sum_{i=1}^m (\frac{d_i}{n_i} \times 92 \times A_i)}{\sum_{i=1}^m A_i}, \quad (5)$$

where d_i , n_i and A_i are the number of days with hazardous humid-heat, the number of days with observations in the summer (June to August) and the area of the i -th C-CU (or C-CR) within the target region, respectively. i ranges from 1 to m , and there are m C-CUs (or C-CRs) in the target region. This equation incorporates area as a weighting factor to reflect the spatial distribution of different regions, ensuring that larger areas contribute proportionately more to the aggregated results. The weighting mechanism allows for a more accurate representation of risk at larger scales, making the results reflective of the true geographical distribution in urban and rural areas.

HI, VI and EI were calculated by Eq. (6):

$$Y' = 0.05 + \frac{Y - \text{MIN}_Y}{\text{MAX}_Y - \text{MIN}_Y} \times (0.95 - 0.05), \quad (6)$$

where Y is the normalized result, that is, HI, VI or EI. Y is the original value of the above three risks (for example, for HI, it is the number of summer hazardous humid-heat days). MIN_Y and MAX_Y are the minimum and maximum values of the original value, respectively. To avoid the mixing of zero values, which would confuse the calculation of subsequent comprehensive risks of hazards, vulnerability, and exposure, normalization was carried out in the range of 0.05–0.95, following approaches used in previous studies⁴³.

Vulnerability is a function of sensitivity and adaptability^{12,44}. In this work, we selected 8 social-ecological indicators to measure vulnerability risk based on 4 SDGs closely related to the humid-heat response (see Selection of sustainable development goals and scoring calculation). These indicators encompassed both sensitivity and capacity aspects (Supplementary Table 1). Principal component analysis (PCA) provides an empirical solution for capturing collinearity among variables through dimensionality reduction and has been widely used in multifactor assessments⁴⁵. It is an exploratory technique that is well suited to the quantitative analysis of the data used in this study, whereas other nonlinear methods applied to such data were overparameterized⁴⁵. In this work, the PCA method was used for assessment of vulnerability risk.

The greater the value of the sensitivity indicator, the weaker the residents' ability to cope with humid-heat risk, indicating stronger vulnerability, while the greater the value of the capacity index, the weaker the vulnerability. Therefore, the sensitivity and capacity indicators were used as positive and negative indicators for vulnerability, respectively. Negative indicators were transformed to align with a positive direction. Each factor was subjected to Z-score standardization. We performed PCA and tested the significance of the PCA dimensions with the R package psych (<https://rdocumentation.org/packages/psych/versions/2.3.3>) and PCAtest⁴⁶, extracting components that were significant at the 0.05 level. The PCA results were normalized with Eq. (6) to obtain the VI.

Exposure refers to people, livelihoods, or economic assets in areas where disasters are likely to occur¹². Exposure measures vary depending on the focus and objectives of the study. We focused on the risks faced by the population, so we characterized exposure risk using population density. The population data were sourced from WorldPop (<https://doi.org/10.5258/SOTON/WP00654>). Population density was calculated by dividing the total population of the target region by its land area. It was normalized using Eq. (6) to obtain the EI.

Data availability

The sources of all the data used are acknowledged in the Methods and Supplementary Table 1. The data underlying the analyses in this study are deposited in the Zenodo repository under <https://doi.org/10.5281/zenodo.17493294>.

Code availability

In this study, panel a of Fig. 1 was generated using the open-source programming languages R. The code is available at the Zenodo repository (<https://doi.org/10.5281/zenodo.17493294>). All other figures were created directly using OriginPro software without the involvement of programming code. The data used for these figures can be found in the Data availability section.

References

1. Lüthi, S. et al. Rapid increase in the risk of heat-related mortality. *Nat. Commun.* **14**, 4894 (2023).
2. Li, D., Yuan, J. & Kopp, R. E. Escalating global exposure to compound heat-humidity extremes with warming. *Environ. Res. Lett.* **15**, 064003 (2020).
3. Raymond, C., Matthews, T. & Horton, R. M. The emergence of heat and humidity too severe for human tolerance. *Sci. Adv.* **6**, eaaw1838 (2020).
4. Dong, J. et al. Trends of the intra-annual onset and end of humid heatwaves in the Northern Hemisphere. *Earth's Future* **12**, e2024EF005163 (2024).
5. Fouillet, A. et al. Has the impact of heat waves on mortality changed in France since the European heat wave of summer 2003? A study of the 2006 heat wave. *Int. J. Epidemiol.* **37**, 309–317 (2008).
6. Barriopedro, D. et al. The hot summer of 2010: redrawing the temperature record map of Europe. *Science* **332**, 220–224 (2011).
7. Dunne, J. P., Stouffer, R. J. & John, J. G. Reductions in labour capacity from heat stress under climate warming. *Nat. Clim. Change* **3**, 563–566 (2013).
8. Parsons, L. A. et al. Global labor loss due to humid heat exposure underestimated for outdoor workers. *Environ. Res. Lett.* **17**, 014050 (2022).
9. Coffel, E. D., Horton, R. M. & de Sherbinin, A. Temperature and humidity based projections of a rapid rise in global heat stress exposure during the 21st century. *Environ. Res. Lett.* **13**, 014001 (2017).
10. Im, E.-S., Pal, J. S. & Eltahir, E. A. B. Deadly heat waves projected in the densely populated agricultural regions of South Asia. *Sci. Adv.* **3**, e1603322 (2017).
11. Wang, S. Q. et al. Health-integrated heat risk assessment in Australian cities. *Environ. Impact Assess. Rev.* **102**, 107176 (2023).
12. Estoque, R. C. et al. Heat health risk assessment in Philippine cities using remotely sensed data and social-ecological indicators. *Nat. Commun.* **11**, 1581 (2020).
13. Savić, S. et al. Heat wave risk assessment and mapping in urban areas: case study for a midsized Central European city, Novi Sad (Serbia). *Nat. Hazards* **91**, 891–911 (2018).
14. World Bank. World Bank Country and Lending Groups. Available at: <https://datahelpdesk.worldbank.org/knowledgebase/articles/906519-world-bank-country-and-lending-groups>. (Accessed: October 13, 2025).
15. Ning, G. et al. Dominant modes of summer wet bulb temperature in China. *Clim. Dyn.* **59**, 1473–1488 (2022).
16. National Bureau of Statistics of China. National Bureau of Statistics Data Query. Available at: <https://data.stats.gov.cn/easyquery.htm?cn=C01&zb=A0305&sj> (Accessed: April 13, 2025).
17. Luo, M. & Lau, N.-C. Urban expansion and drying climate in an urban agglomeration of East China. *Geophys. Res. Lett.* **46**, 6868–6877 (2019).
18. Huang, S. et al. Urbanization amplified asymmetrical changes of rainfall and exacerbated drought: analysis over five urban agglomerations in the Yangtze River Basin, China. *Earth's Future* **11**, e2022EF003117 (2023).
19. Li, Y., Schubert, S., Kropp, J. P. & Rybski, D. On the influence of density and morphology on the Urban Heat Island intensity. *Nat. Commun.* **11**, 2647 (2020).
20. Ji, J. S. et al. China's public health initiatives for climate change adaptation. *Lancet Reg. Health West. Pac.* **40**, 100965 (2023).
21. Song, Y. et al. Developing an indicator system and assessing China's progress on climate change adaptation in 2010–2022 from dual-dimension. *Environ. Sustain. Indic.* **26**, 100613 (2025).
22. Wang, P. et al. Extreme wet-bulb temperatures in China: the significant role of moisture. *J. Geophys. Res. Atmos.* **124**, 11944–11960 (2019).
23. Li, C. et al. Rapid warming in summer wet bulb globe temperature in China with human-induced climate change. *J. Clim.* **33**, 5697–5711 (2020).

24. Zhang, K. et al. Increased heat risk in wet climate induced by urban humid heat. *Nature* **617**, 738–742 (2023).

25. Mishra, V. et al. Moist heat stress extremes in India enhanced by irrigation. *Nat. Geosci.* **13**, 722–728 (2020).

26. Ding, Y. & Chan, J. C. L. The East Asian summer monsoon: an overview. *Meteorol. Atmos. Phys.* **89**, 117–142 (2005).

27. Zhou, X., Ding, Y. & Wang, P. Moisture transport in the Asian summer monsoon region and its relationship with summer precipitation in China. *J. Meteorol. Res.* **24**, 31–42 (2010).

28. Du, J. et al. Effects of rapid urbanization on vegetation cover in the metropolises of China over the last four decades. *Ecol. Indic.* **107**, 105458 (2019).

29. Gong, P., Li, X. & Zhang, W. 40-Year (1978–2017) human settlement changes in China reflected by impervious surfaces from satellite remote sensing. *Sci. Bull.* **64**, 756–763 (2019).

30. He, C. et al. Estimating spatial effects of anthropogenic heat emissions upon the urban thermal environment in an urban agglomeration area in East China. *Sustain. Cities Soc.* **57**, 102046 (2020).

31. Chen, J. et al. The influences of aging population and economic growth on Chinese rural poverty. *J. Rural Stud.* **47**, 665–676 (2016).

32. Gao, S. et al. Urbanization-induced warming amplifies population exposure to compound heatwaves but narrows exposure inequality between global North and South cities. *npj Clim. Atmos. Sci.* **7**, 154 (2024).

33. Klein, T. & Anderegg, W. R. L. A vast increase in heat exposure in the 21st century is driven by global warming and urban population growth. *Sustain. Cities Soc.* **73**, 103098 (2021).

34. Tuholske, C. et al. Global urban population exposure to extreme heat. *Proc. Natl. Acad. Sci. USA* **118**, e2024792118 (2021).

35. Chen, M. et al. Population distribution and urbanization on both sides of the Hu Huanyong Line: answering the Premier's question. *J. Geogr. Sci.* **26**, 1593–1610 (2016).

36. Wang, H. & Ge, Q. Spatial association network of economic resilience and its influencing factors: evidence from 31 Chinese provinces. *Hum. Soc. Sci. Commun.* **10**, 1–14 (2023).

37. Knauer, J. et al. Bigleaf—An R package for the calculation of physical and physiological ecosystem properties from eddy covariance data. *PLoS ONE* **13**, e0202114 (2018).

38. Jeong, J. et al. Identifying outliers of non-Gaussian groundwater state data based on ensemble estimation for long-term trends. *J. Hydrol.* **548**, 135–144 (2017).

39. Xu, C. et al. Improvement and optimization of coal dust concentration detection technology: based on the 3σ criterion and the Kalman filtering composite algorithm. *Flow Meas. Instrum.* **97**, 102598 (2024).

40. Liu, Z. et al. Surface warming in global cities is substantially more rapid than in rural background areas. *Commun. Earth Environ.* **3**, 219 (2022).

41. Beck, H. et al. High-resolution (1 km) Köppen–Geiger maps for 1901–2099 based on constrained CMIP6 projections. *Sci. Data* **10**, 724 (2023).

42. Xu, Z. et al. Assessing progress towards sustainable development over space and time. *Nature* **577**, 74–78 (2020).

43. Dong, J. et al. Heatwave-induced human health risk assessment in megacities based on heat stress–social vulnerability–human exposure framework. *Landsc. Urban Plan.* **203**, 103907 (2020).

44. IPCC. Summary for Policymakers. In *Climate Change 2014: Impacts, Adaptation, and Vulnerability. Part A: Global and Sectoral Aspects*, Contribution of Working Group II to the Fifth Assessment Report of the Intergovernmental Panel on Climate Change (Cambridge Univ. Press, 2014).

45. Migliavacca, M. et al. The three major axes of terrestrial ecosystem function. *Nature* **598**, 468–472 (2021).

46. Camargo, A. PCAtest: testing the statistical significance of Principal Component Analysis in R. *PeerJ* **10**, e12967 (2022).

47. Rui, C., Zhang, H. & Chen, B. China temporal administrative map: a multitemporal database for Chinese historical administrative divisions (2009–2023). In *Proc. Third International Conference on Environmental Remote Sensing and Geographic Information Technology (ERSGIT 2024)* Vol. 13565, 497–507 (SPIE, 2025).

Acknowledgements

This study was supported by the National Natural Science Foundation of China through Grant 42421001 (S.C.), Grant 42595595 (S.C. and L.L.) and Grant 423B2506 (C.L.), the National Natural Science Foundation of China and the China Meteorological Administration through Grant U2242209 (S.C.), the Major Science and Technology Special Project of Gansu Province through Grant 25ZDFA008 (S.C., Y.J., L.L. and N.Y.) and by the National Natural Science Foundation of China through Grant 42175106 (S.C.).

Author contributions

C.L., S.C., and J.H. designed the study. C.L. conducted the simulations and analysis. X.L., C.Z., K.Z., L.L. and Y.J. contributed to the determination of the research direction in the early stages. X.T. downloaded the data and C.L. and S.C. contributed to the writing and discussed the results. L.L., N.Y., and R.Z. collected, organized, and analyzed the literature. D.W. refined and edited the language of the article.

Competing interests

The authors declare no competing interests.

Additional information

Supplementary information The online version contains supplementary material available at <https://doi.org/10.1038/s41467-025-67558-y>.

Correspondence and requests for materials should be addressed to Siyu Chen.

Peer review information *Nature Communications* thanks Fengqi Cui, Jiaxi Yang, Nurul Syahira Mohammad Harmay and the other anonymous, reviewer(s) for their contribution to the peer review of this work. A peer review file is available.

Reprints and permissions information is available at <http://www.nature.com/reprints>

Publisher's note Springer Nature remains neutral with regard to jurisdictional claims in published maps and institutional affiliations.

Open Access This article is licensed under a Creative Commons Attribution-NonCommercial-NoDerivatives 4.0 International License, which permits any non-commercial use, sharing, distribution and reproduction in any medium or format, as long as you give appropriate credit to the original author(s) and the source, provide a link to the Creative Commons licence, and indicate if you modified the licensed material. You do not have permission under this licence to share adapted material derived from this article or parts of it. The images or other third party material in this article are included in the article's Creative Commons licence, unless indicated otherwise in a credit line to the material. If material is not included in the article's Creative Commons licence and your intended use is not permitted by statutory regulation or exceeds the permitted use, you will need to obtain permission directly from the copyright holder. To view a copy of this licence, visit <http://creativecommons.org/licenses/by-nc-nd/4.0/>.

© The Author(s) 2025